AAAS
Research
Volume 2019, Article ID 8078549, 11 pages
https://doi.org/10.34133/2019/8078549

Research
OFFICIAL JOURNAL OF CAST

Research Article

Synthesis of PdS_x- Mediated Polydymite Heteronanorods and Their Long-Range Activation for Enhanced Water Electroreduction

Qiang Gao[1], Rui Wu[1], Yang Liu[1], Ya-Rong Zheng[1], Yi Li[1], Li-Mei Shang[1], Yi-Ming Ju[1], Chao Gu[1], Xu-Sheng Zheng[2], Jian-Wei Liu[1], Jun-Fa Zhu[2], Min-Rui Gao[1], and Shu-Hong Yu[1,3]

[1]*Division of Nanomaterials & Chemistry, Hefei National Laboratory for Physical Sciences at the Microscale, CAS Center for Excellence in Nanoscience, Hefei Science Center of CAS, Collaborative Innovation Center of Suzhou Nano Science and Technology, Department of Chemistry, University of Science and Technology of China, Hefei 230026, China*
[2]*National Synchrotron Radiation Laboratory, University of Science and Technology of China, Hefei 230026, China*
[3]*Dalian National Laboratory for Clean Energy, Dalian 116023, China*

Correspondence should be addressed to Min-Rui Gao; mgao@ustc.edu.cn and Shu-Hong Yu; shyu@ustc.edu.cn

Received 24 February 2019; Accepted 13 May 2019; Published 18 August 2019

Copyright © 2019 Qiang Gao et al. Exclusive Licensee Science and Technology Review Publishing House. Distributed under a Creative Commons Attribution License (CC BY 4.0).

Material interfaces permit electron transfer that modulates the electronic structure and surface properties of catalysts, leading to radically enhanced rates for many important reactions. Unlike conventional thoughts, the nanoscale interfacial interactions have been recently envisioned to be able to affect the reactivity of catalysts far from the interface. However, demonstration of such unlocalized alterations in existing interfacial materials is rare, impeding the development of new catalysts. We report the observation of unprecedented long-range activation of polydymite Ni_3S_4 nanorods through the interfacial interaction created by PdS_x nanodots (dot-on-rod structure) for high-performance water catalytic electroreduction. Experimental results show that this local interaction can activate Ni_3S_4 rods with length even up to 25 nanometers due to the tailored surface electronic structure. We anticipate that the long-range effect described here may be also applicable to other interfacial material systems, which will aid the development of newly advanced catalysts for modern energy devices.

1. Introduction

It has been almost 46 years since the proposition of the *hydrogen economy* concept, which depicted a clean, safe, and sustainable alternative to the current hydrocarbon economy [1]. Recent research has led to many advances towards this blueprint, but large-scale hydrogen production through electrocatalysis at low overpotentials (η) remains a challenge [2]. Although expensive precious metals such as platinum capable of catalyzing the hydrogen evolution reaction (HER) at fast rates are known, the reliable and scalable electrolyzers require low-cost and efficient catalysts based on geologically abundant elements [3, 4]. In conventional heterogeneous catalysis, an intuitive and commonly used method towards better catalysts is to couple transition metal nanoparticles with oxide or carbon supports, which creates the so-called 'strong metal-support interactions' that modulate the electronic structure and surface properties of catalytic materials, leading to enhanced performances [5–14]. This interaction-induced phenomena has been extensively studied since being discovered by Tauster et al. in 1970s [14], which is now understood to be due to the electron transfer across the formed interfaces [7]. Lykhach and coworkers have quantified the electron transfer experimentally on a Pt-CeO_2 catalyst and observed a characteristic particle size dependence [7]. Commonly, such interaction is thought to be localized at the subnanometre scale, suggesting that only reactive sites in the immediate vicinity of the interface are influenced [5, 15]. Very recently, Suchorski and coworkers' study with Pd-metal oxide catalysts, however, demonstrated that the interfacial interaction can activate the CO oxidation energetics of Pd sites thousands of nanometers away from the interface [5]. In recent years, material interface engineering has also led to substantial advances in

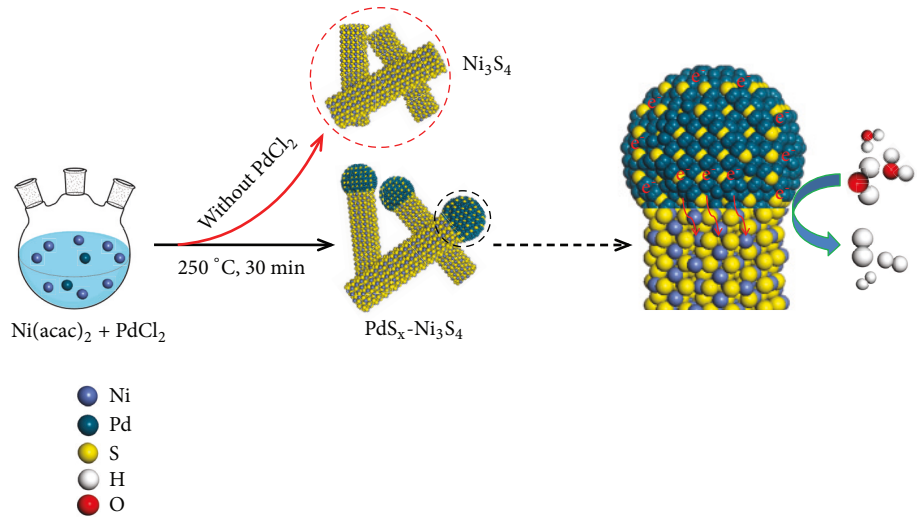


FIGURE 1: *The synthesis of PdS_x-Ni_3S_4 heteronanorods.* Schematic illustration of the synthesis of the PdS_x-Ni_3S_4 heteronanorods, showing PdS_x mediates the electronic structure of polydymite Ni_3S_4. Blue, yellow, and cyan balls correspond to Ni, S, and Pd atoms, respectively.

designing electrocatalysts via the interface-created structural perturbations [16–18]. Nonetheless, whether the long-range activation phenomenon exists in these interfacial electrocatalyst systems, for example, the heterostructures, remains unknown and needs to be clarified experimentally, which could be complementary for understanding the interface-induced enhancement behavior and yield better performing HER electrocatalysts.

In nature, hydrogenases are able to catalyze the HER at potentials close to its thermodynamic value ($2H^+ + 2e^- \longrightarrow H_2$; 0-0.059 × pH, V versus normal H_2 electrode at 298 K), despite using cheap metals, such as nickel, iron, and molybdenum, as active sites [19]. This leads to investigations of inorganic analogues or complexes that mimic such active centers as catalysts for HER, for example, the representative molybdenite MoS_2 [20–22]. Besides molybdenum, chalcogenides of many other elements, such as iron [23, 24], cobalt [25–28], and nickel [23, 24, 29], have also shown significant potentials in HER electrocatalysis. Of these, nickel sulfides are particularly intriguing because they can form various phases such as NiS, NiS_2, Ni_3S_2, Ni_3S_4, Ni_7S_6, and Ni_9S_8 that offer diverse properties [30], and because they had demonstrated good uses as electrode materials for Li-ion batteries [31–33], supercapacitors [34–36], and catalysts for hydrodesulfurization reactions [37]. Previous works were focused primarily on heazlewoodite Ni_3S_2 [29, 38], which holds promise for electrocatalysis of oxygen reduction [39] and hydrogen evolution [29]; but studies on other nickel sulfides are comparatively rare, leaving their catalytic properties largely unexplored. For example, polydymite Ni_3S_4 is a common mineral existed in ores, which crystallizes in cubic spinel structure with Ni^{2+}/Ni^{3+} couple [40, 41]. Although interesting structure, methods of synthesizing nanostructured Ni_3S_4 often lead to significant phase impurity [42], which hampers the technological exploitation of Ni_3S_4 as a HER catalyst, even though both nickel and sulfur are essential to hydrogenases [19]. Yet engineering these metal chalcogenides, for example, the activation of single phase Ni_3S_4 via interfacial interactions, that aims for high-performance HER catalysis is even more challenging.

Herein, we report the synthesis of high-pure Ni_3S_4 nanorods mediated with nanoparticulate PdS_x on the tip of each nanorod, where the resulting PdS_x-Ni_3S_4 interface shows an unprecedented long-range effect on the reactivity of Ni_3S_4 in water catalytic electroreduction. PdS_x was the material of choice because it is conductive and chemically robust under harsh conditions such as low pH and high temperature [43]. We reveal that such interfacial interaction enables the activation of Ni_3S_4 nanorods with length up to 25 nm, making the PdS_x-Ni_3S_4 a highly active and stable HER catalyst. We understand the interaction-induced enhancement based on a range of experimental investigations and propose that remarkable charge transfer across the PdS_x-Ni_3S_4 interface enables surface structural optimization of Ni_3S_4 nanorods, giving rise to the catalytic promotions. These findings may be potentially applied to other material systems and lead to broader libraries of interfacial catalysts for reactions beyond H_2 evolution.

2. Results

2.1. Synthesis and Structural Characterizations of the PdS_x-Ni_3S_4 Heteronanorods. We achieved the synthesis of well-defined, pure-phase Ni_3S_4 nanorods functionalized with nanoparticulate PdS_x terminations (i.e., dot-on-rod structure) by consecutive thermolysis of corresponding metal precursors, as illustrated schematically in Figure 1. Briefly, $[Ni(acac)_2]$ (acac = acetylacetonate) and $PdCl_2$ were mixed in a solution containing 1-dodecanethiol (DDT) and oleylamine (OAm), which was then heated to 250°C and maintained for 30 minutes. In the synthesis of the PdS_x-Ni_3S_4 colloidal heteronanorods, DDT acts as the sulfur source, while OAm acts as both the solvent and stabilizer. Transmission electron microscopy (TEM) image of the as-synthesized sample

reveals uniform 'dot-on-rod'-like structures with the dot size of ~6.8 nm, as well as the rod length and diameter of ~ 25.1 nm and ~6.7 nm, respectively (Figures 2(a)–2(c)). High-angle annular dark-field scanning TEM (HAADF-STEM, Figure 2(d) and inset) image clearly shows the 'dot-on-rod' heterostructure that corresponds to PdS_x (bright) and Ni_3S_4 (gray), respectively, owing to the Z^2-dependent contrast (Z is the atomic number). Studies with high-resolution TEM (HRTEM, Figure 2(e)) demonstrate good crystallinity of Ni_3S_4 nanorods with resolved lattice fringe of (113) plane, which are free from any secondary phases, whereas the PdS_x dot presents as unexpected amorphous phase (Figures 2(e), S1, and S2). The fast Fourier transform (FFT) patterns taken from the dashed circles again evidence the crystalline (Figure 2(f)) and amorphous (Figure 2(g)) structures, respectively. We further confirmed this through X-ray diffraction (XRD) studies of the product (Figure 2(h), red curve), in which the strong diffraction peaks are assigned to cubic Ni_3S_4 with spinel structure (JCPDS No. 43-1469). Our XRD studies show almost negligible peak at 37.5° resulting from the amorphous PdS_x (Figure 2(h), red and blue curves) [44], consistent with the above observations. Energy-dispersive X-ray spectroscopy (EDS) confirms the expected chemical elements although it picked up Cu and C signals from the TEM grid (Figure S3). STEM elemental mapping of the PdS_x-Ni_3S_4 sample shows Pd-rich dots and Ni-rich rods with S enrichment in the whole structure (Figures 2(i) and S4), matching well with our EDS line scan that passes through the central axis of a typical heteronanorod (Figure S5). We have also determined that the molar content of PdS_x in PdS_x-Ni_3S_4 heteronanorods is about 10.5% based on the inductively coupled plasma mass spectrometer (ICP-MS) studies, which agrees with the ~10% value measured by EDS. Together, these results support that we have succeeded in synthesizing the new, uniform, and high-pure PdS_x-Ni_3S_4 heteronanorods.

We designed and conducted a series of control experiments to explore the formation of PdS_x-Ni_3S_4 heteronanorods. By varying the amount of 1-dodecanethiol we can effectively tune the length of Ni_3S_4 nanorods in the 'dot-on-rod' structure. For example, adding 0.25 mL 1-dodecanethiol into the reaction system results in Ni_3S_4 nanorods with length of ~15 nm, which substantially increases to ~25.1 and ~ 34.8 nm after addition of 0.5 and 0.6 mL 1-dodecanethiol, respectively (Figure S6). However, no large growth for the PdS_x nanoparticles was seen in these experiments. Further, increasing the amount of 1-dodecanethiol yields PdS_x-Ni_3S_4 heterostructure with rod coarsening, while a lower addition of 0.1 mL gives spherical nanoparticles instead of nanorods (Figure S7). These observations indicate that the size and shape of Ni_3S_4 are controlled via 1-dodecanethiol. As to PdS_x, we found that its growth shows a pronounced temperature dependence. Reaction at temperature of 230°C results in dominant Ni_3S_4 nanorods without PdS_x, suggesting the high formation energy of PdS_x species. But too much thermal input (e.g., 270°C) induces isotropic growth, forming nonuniform nanoparticles (Figure S8). We determined the appropriate temperature for synthesizing PdS_x-Ni_3S_4 heteronanorods is 250°C. Moreover, Pd:Ni molar ratio in the reaction system is also critical and the best value was uncovered to be 1:4. Deviating from this value will make the product form irregular or nonuniform structures (Figure S9). We carefully examined the samples at different stages during the synthesis by TEM to probe the evolutionary process of PdS_x-Ni_3S_4 heteronanorods (Figure S10). Rod-like product appeared when the mixture reached 250°C, but without PdS_x terminations. At early stage (5 min), particulate PdS_x started to emerge at the tip of each nanorod, which grew in size as the reaction proceeded, forming optimal PdS_x-Ni_3S_4 heteronanorods at 30 min. These observations are somewhat similar to the synthesis of anisotropically phase-segregated PdS_x-Co_9S_8 and PdS_x-Co_9S_8-PdS_x nanoacorns reported previously by Teranishi and coworkers [44, 45]. We further note that if no Pd precursor was provided, pure Ni_3S_4 nanorods would result (Figures S11 and S12); if without Ni addition, nanoparticulate PdS_x would form, but at a higher temperature of 300°C (Figures S13c-d). Lower temperature such as 250°C gives yellow Pd precursor with unknown phase (Figures S13a-b). However, in the PdS_x-Ni_3S_4 growth system, the preformed Ni_3S_4 nanorods can allow heterogeneous nucleation of PdS_x on their tips to substantially lower the nucleation barrier, which permits the formation of PdS_x-Ni_3S_4 at lower temperature of mere 250°C. Because of the deficient energy for crystallization, the PdS_x nanodots on the tips show the amorphous nature.

2.2. Interactions between PdS_x Nanoparticles and Ni_3S_4 Nanorods. The electronic interactions between PdS_x nanoparticles and Ni_3S_4 nanorods were comprehensively investigated via multiple characterization techniques (Figures 3 and S14). X-ray photoelectron spectroscopy (XPS) measurements show that the binding energy of Ni 2*p* core levels markedly decreases by ~0.96 eV versus pure Ni_3S_4, attributable to charge transfer from PdS_x to Ni_3S_4 (Figure 3(a)). We highlight that this chemical shift of Ni 2*p* peak is remarkable, which can not solely originate from the local nanoscale PdS_x-Ni_3S_4 interface, but remote surfaces of Ni_3S_4 in these heteronanorods should be also affected. Such charge transfer is further confirmed by the shift of absorption edge towards lower energy in X-ray absorption near-edge spectroscopy (XANES) of the Ni *K*-edge (Figure 3(b)). Additionally, the decrease in the white line intensity again verifies that Ni_3S_4 accepts electrons from PdS_x in the heteronanorods (Figure 3(b)). Figure 3(c) presents Fourier-transformed Ni K-edge extended X-ray absorption fine structure (EXAFS) analysis for studied materials. Features that correspond to the nearest Ni-S coordination (~1.66 Å) are clearly seen for both PdS_x-Ni_3S_4 and pure Ni_3S_4, whereas the peak intensity increases for PdS_x-Ni_3S_4. This indicated that the outer shell of the Ni centers in PdS_x-Ni_3S_4 definitely changed compared to that of Ni_3S_4 [46]. S *K*-edge XANES spectra in Figure 3(d) show a broad peak at ~2472.0 eV that attributed to characteristic S^{2-}, which locates between pure PdS_x (~2471.4 eV) and Ni_3S_4 (~2472.6 eV), indicating that the S electronic environment was neutralized in PdS_x-Ni_3S_4 heteronanorods because of the electron transfer from PdS_x to Ni_3S_4 [47–49]. By using electron energy-loss spectroscopy (EELS) in the STEM mode, we measured the L_3/L_2 ratio at Ni *L*-edge far

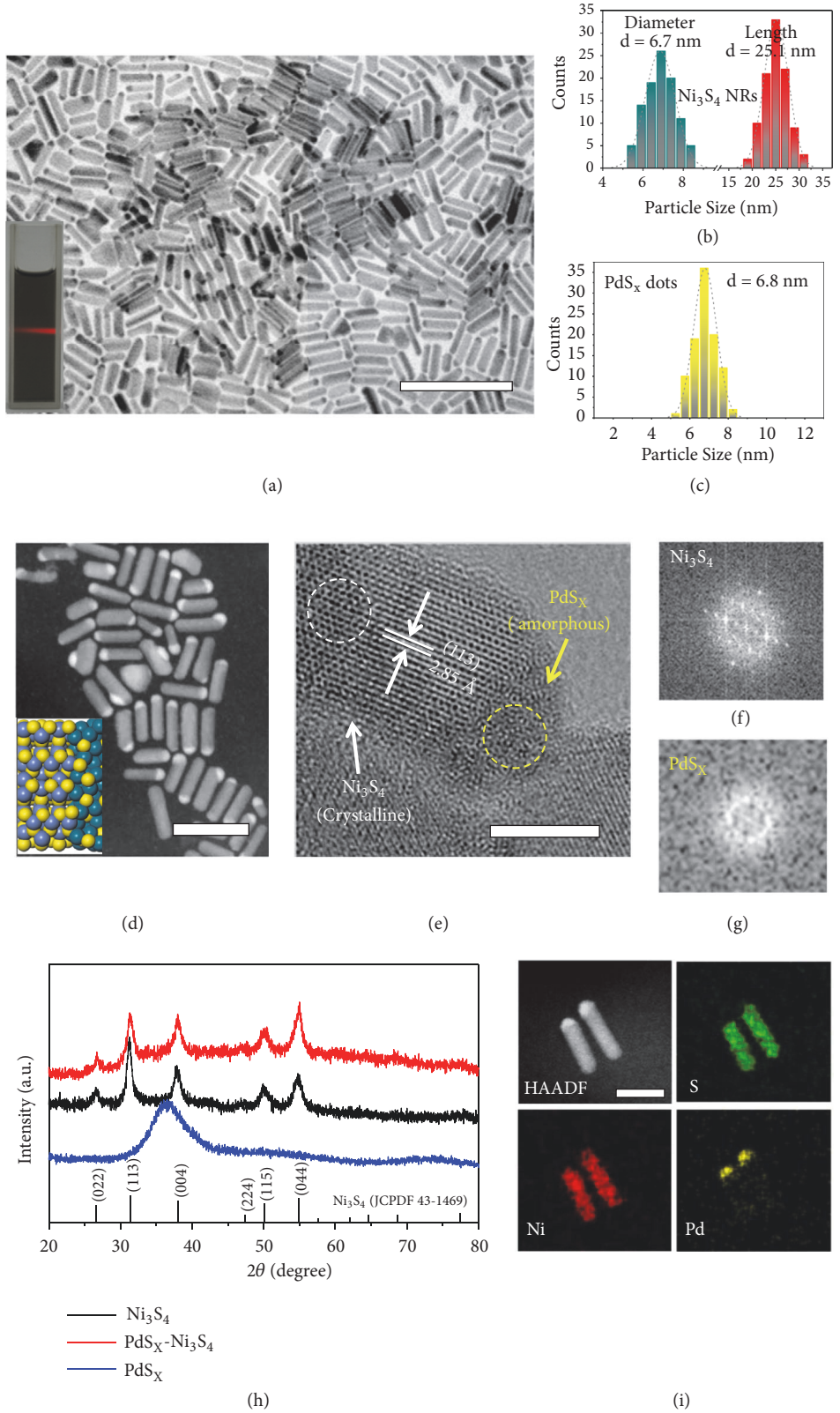


FIGURE 2: *Characterizations of the PdS_x-Ni_3S_4 heteronanorods.* (a) TEM image of synthesized PdS_x-Ni_3S_4 heteronanorods. Scale bar, 50 nm. A digital image of PdS_x-Ni_3S_4 heteronanorods in hexane is shown as inset. (b and c) Histograms of PdS_x-Ni_3S_4 heteronanorods showing the size of Ni_3S_4 nanorods and PdS_x dots, respectively. (d) HAADF-STEM image of PdS_x-Ni_3S_4 heteronanorods. Scale bar, 20 nm. Inset gives the crystal structure of PdS_x-Ni_3S_4. Blue, yellow, and cyan balls correspond to Ni, S, and Pd atoms, respectively. (e) HRTEM image of a typical PdS_x-Ni_3S_4 heteronanorod. Scale bar, 5 nm. (f and g) The FFT patterns taken from the regions marked by white and yellow dashed circles of (e), featuring the crystalline Ni_3S_4 and amorphous PdS_x, respectively. (h) XRD patterns of PdS_x-Ni_3S_4 heteronanorods, pure Ni_3S_4, and PdS_x. (i) HAADF image and STEM elemental mapping of PdS_x-Ni_3S_4 heteronanorods. Scale bar, 20 nm.

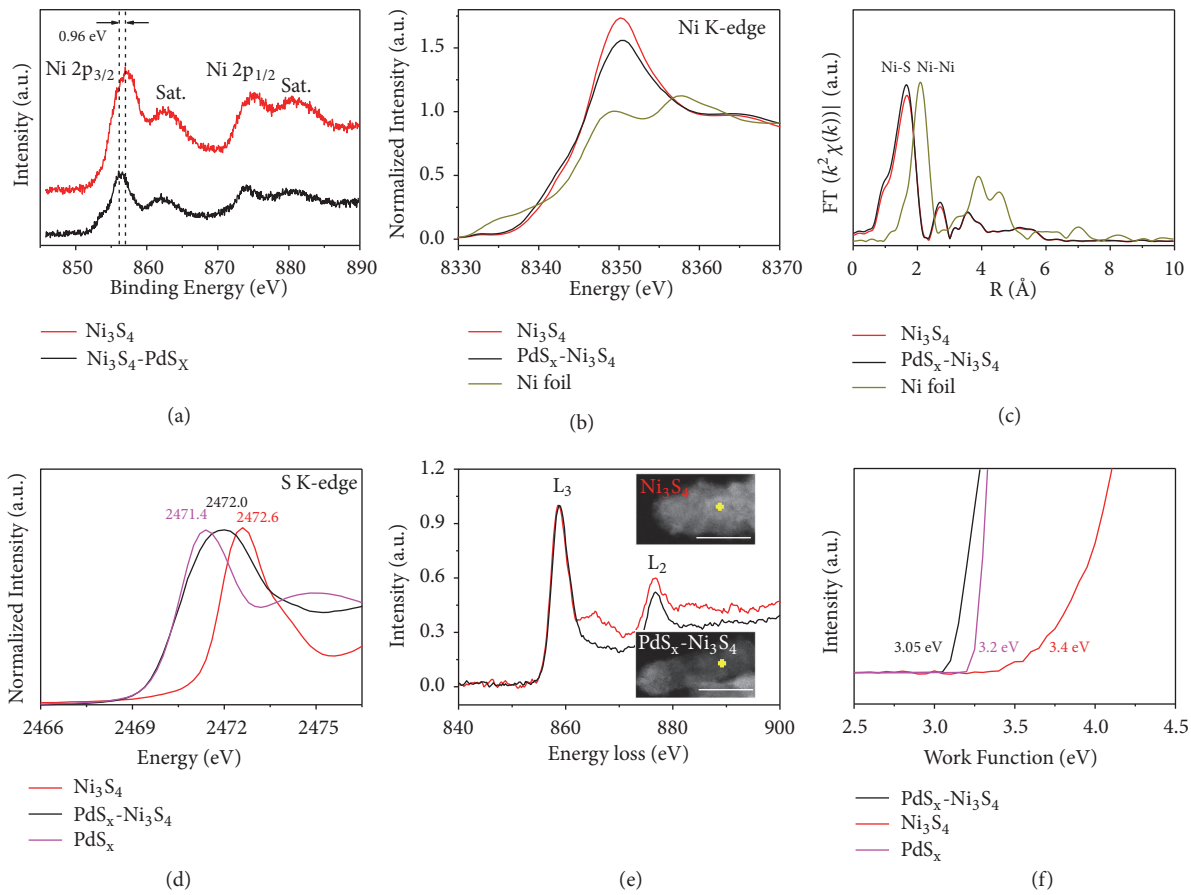


FIGURE 3: *Electronic structure modulation in PdS_x-Ni_3S_4 heteronanorods.* (a) Ni 2*p* XPS spectra of PdS_x-Ni_3S_4 and pure Ni_3S_4, showing a decrease of ~0.96 eV after coupling Ni_3S_4 with PdS_x. (b) Ni *K*-edge XANES spectra of PdS_x-Ni_3S_4, Ni_3S_4, and Ni foil reference. (c) EXAFS Fourier-transformed k^3-weighted $\chi(k)$ function spectra of PdS_x-Ni_3S_4, Ni_3S_4 and Ni foil reference. (d) S *K*-edge XANES spectra of PdS_x-Ni_3S_4, pure Ni_3S_4, and PdS_x. (e) EELS spectra of PdS_x-Ni_3S_4 and Ni_3S_4 at Ni *K*-edge. Insets show the representative positions of EELS acquisition. Scale bars, 10 nm. (f) Ultraviolet photoelectron spectra of PdS_x-Ni_3S_4, pure Ni_3S_4, and PdS_x.

away from the rod ends (Figure 3(e) and Insets). Expectedly, we see noticeable larger L_3/L_2 ratio for PdS_x-Ni_3S_4 versus pure Ni_3S_4, adding further strong support to our finding that long-range electronic modulation can be enabled by the nanoscale interface.

On the basis of this set of experiments we demonstrate clear long-range impact on surface features in the PdS_x-Ni_3S_4 case as compared with pure Ni_3S_4. Furthermore, ultraviolet photoelectron spectroscopy (UPS; Figure 3(f)) measurements reveal that PdS_x-Ni_3S_4 heteronanorods possess lower work function (3.05 eV) relative to metallic PdS_x (3.2 eV) and pure Ni_3S_4 (3.4 eV). These results offer additional evidence that superior electronic property is gained because of the long-range effect of the nanoscopic interface (Figure 4(a)).

2.3. Long-Range Activation in the PdS_x-Ni_3S_4 Heteronanorods. The long-range activation of Ni_3S_4 nanorods via the PdS_x-Ni_3S_4 interfaces was experimentally demonstrated by evaluating their HER activity in N_2-saturated 0.5 M H_2SO_4, with that of pure PdS_x, Ni_3S_4 and Pt/C benchmark for comparison (see Experimental Section). Before electrochemical studies, all of the adsorbed OAm was thoroughly removed by treating the as-synthesized PdS_x-Ni_3S_4 heteronanorods in acetic acid at 70°C for 10 h (Figure S15). We achieved the optimal PdS_x-Ni_3S_4 heterocatalyst for comparative study based on a series of control experiments (Figures S16 and S17). Figure 4(b) reveals that the background HER current from the carbon paper support is featureless, while the same cathodic sweep of PdS_x-Ni_3S_4 heteronanorods (~25 nm) exhibits a sharp current jump at about -20 mV versus reversible hydrogen electrode (RHE), accounting for the catalytic HER. In contrast, pure Ni_3S_4 starts the HER at larger η of 120 mV, whereas free PdS_x nanoparticles offer negligible HER activity. At a current density of 10 mA cm^{-2}, the recorded η for PdS_x-Ni_3S_4 was mere 63 mV versus greatly larger η of 304 mV for pure Ni_3S_4 (Figure 4(b)). These results clearly reveal that Ni_3S_4 nanorods are inherently activated through coupling with PdS_x for superior HER energetics, exceeding previously reported performances of other Ni-based HER catalysts (Figures 4(c) and S18). Steady-state current densities as a function of η (that is, $\log j \sim \eta$) were recorded to probe useful kinetic metrics of studied catalysts, as shown in Figure 4(d). Tafel slope of ~45 mV per decade was measured for PdS_x-Ni_3S_4, which is smaller

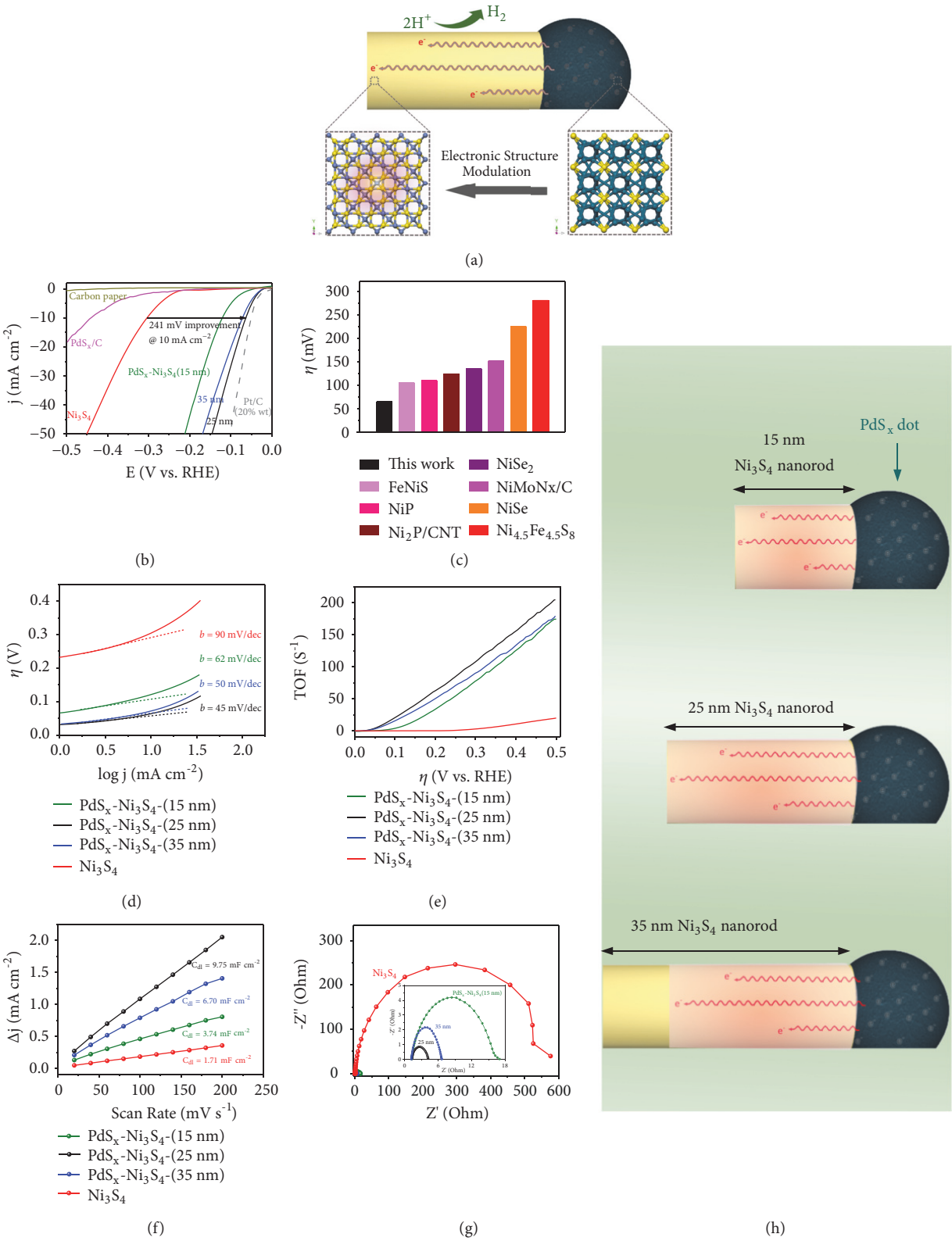


FIGURE 4: *Water electroreduction evaluation.* (a) Schematic of the long-range activation in PdS_x-Ni_3S_4 heteronanorod. A PdS_x dot coupled with Ni_3S_4 nanorod to form the strong interfacial interaction that permits remote electronic structure modulation of Ni_3S_4, leading to enhanced electrocatalytic properties. (b) Polarization curves for HER of different studied catalysts. Catalyst loading: 1 mg cm^{-2}. Sweep rate: 5 mV s^{-1}. (c) Comparison of η required to yield a current density of 10 mA cm^{-2} on various Ni-based electrocatalysts. (d) Tafel plots for the different catalysts derived from (b). (e) TOF as a function of η for different catalysts. (f) Plots showing the extraction of the C_{dl} for different catalysts. (g) EIS Nyquist plots of different catalysts. Inset compares Nyquist plots at high-frequency range for PdS_x-Ni_3S_4 heteronanorods with different rod lengths. Z' is the real impedance and $-Z''$ is the imaginary impedance. *The potential for the Nyquist plot measurement was -0.204 V* versus *RHE.* (h) Schematic of the modulated surface electronic structures of PdS_x-Ni_3S_4 heteronanorod, revealing that the interfacial interaction enable the activation of Ni_3S_4 nanorod up to ~25 nm away from the interface.

than that of other catalysts except for the Pt/C benchmark (Figure S19), demonstrating its efficient HER kinetics. In acid, such a Tafel slope hints at a two-electron transfer process involved Volmer-Tafel mechanism [2]. We further studied the inherent HER activities of these catalysts by calculating their exchange current densities (j_0; Figure S20). The obtained j_0 of 5.62×10^{-2} mA cm^{-2} for PdS_x-Ni_3S_4 makes it a remarkable HER catalyst that heads for the Pt/C benchmark (Table S1). Moreover, the turnover frequency (TOF) of H_2 molecules evolved per second was calculated to be 108 s^{-1} at -300 mV for the PdS_x-Ni_3S_4, substantially exceeding the pure Ni_3S_4 with TOF of 3.2 s^{-1} (Figure 4(e)).

Additional evidence that PdS_x-Ni_3S_4 heterocatalyst gives promoted HER reactivity was demonstrated with the double-layer capacitance (C_{dl}), which is proportional to the effective electrochemically active surface area [50] (Figures 4(f), S21, and S22). The measured large C_{dl} of 9.75 mF cm^{-2} for PdS_x-Ni_3S_4 heterocatalyst implies its high exposure of catalytic active sites, comparing favorably with that of 1.71 mF cm^{-2} for pure Ni_3S_4. Electrochemical impedance spectroscopy (EIS) was next recorded at a η of 200 mV to probe the charge transfer resistance (R_{ct}) for studied catalysts (Figure 4(g)). The measured R_{ct} of 3.1 Ohm for PdS_x-Ni_3S_4 is considerably lower than that for pure Ni_3S_4 (537.2 Ohm), which indicates superior Faradaic process of PdS_x-Ni_3S_4 heterocatalyst, in agreement with our work function measurements presented above (Figure 3(f)).

Our measurement of the superior HER activity on PdS_x-Ni_3S_4 heteronanorods implies a long-range effect of the PdS_x-Ni_3S_4 interface on the reactivity of Ni_3S_4 nanorods. We consider that the enhanced energetics do not originate exclusively from the localized nanoscale interface. Rather, remote Ni_3S_4 surface is activated resulting from the greatly modulated electronic structure discussed in Figure 3. Such pronounced modulation is unlikely to realize by the small population of accessible interfaces in PdS_x-Ni_3S_4 heteronanorods. We further ascertain the enhancement that results from the long-range activation rather than the nanoscale interface by comparing the HER properties for the aforementioned size series of heteronanorods with Ni_3S_4 mean length of 15.0 nm, 25.1 nm, and 34.8 nm. We observe abrupt increase in HER activity for different sized heteronanorods relative to pure Ni_3S_4 nanorods (Figures 4(b)–4(g)), indicating substantial activation of Ni_3S_4 induced by PdS_x. In Figures 4(b)–4(g), our electrochemical measurements also uncover an activity trend of PdS_x-Ni_3S_4 heteronanorods (25.1 nm) > PdS_x-Ni_3S_4 (34.8 nm) > PdS_x-Ni_3S_4 (15.0 nm). This trend of experimental activities suggests that Ni_3S_4 nanorods are able to be activated up to ~25 nm away from the interface (Figure 4(h)). It is clear that, at the same mass loading of the PdS_x-Ni_3S_4 heteronanorods, shorter Ni_3S_4 nanorods (15.0 nm) bring excess inactive PdS_x but longer Ni_3S_4 nanorods (34.8 nm) are mere partially activated. More proportional of inactive PdS_x (in shorter heteronanorods) and unactivated Ni_3S_4 (in longer heteronanorods) both lead to inferior activities. These results give conclusive experimental evidence that long-range activation enabled by interfacial interaction is indeed realized in the PdS_x-Ni_3S_4 heterocatalyst.

2.4. Performance Stability. We now turn to assess the chemical and structural stability of the new PdS_x-Ni_3S_4 heterocatalyst. In Figure 5(a) we show the long-term CV cycling data, which reveals only negligible decay after 2,000 cycles between -200 and 200 mV versus RHE. This observation is in agreement with our EIS measurements, where the Nyquist plots exhibit a mere 0.33 Ohm increase of R_{ct} after cycling (Inset in Figure 5(a)). We performed further stability test by running the HER on PdS_x-Ni_3S_4 heterocatalyst under currents from 10 to 200 mA cm^{-2} continuously for 24 hours. No appreciable increase in η is seen in Figure 5(b), even at the high current density of 200 mA cm^{-2}, underscoring its striking robustness. After electrolysis cycles, the catalyst was removed from carbon paper and characterized by TEM, EDS and elemental mapping, which show that the 'dot-on-rod' structure is maintained with previous elemental distribution (Figures 5(c) and S23). Furthermore, our XPS analysis reveals no obvious chemical state changes after stability test (Figure S24). The above results illustrate the remarkable performing stability of the new PdS_x-Ni_3S_4 heterocatalysts, suggesting the potential electrode application. We finally detected the catalytic generation of H_2 on PdS_x-Ni_3S_4 electrode by gas chromatography, which is consistent with the theoretical value, corresponding to a Faradaic efficiency of ~100% (Figure 5(d)).

3. Discussion

Strong interfacial interaction that leads to enhanced catalytic properties was widely affirmed in metal-support (e.g., oxides) heterogeneous catalysts [5–14]. As mentioned above, such interaction involves charge transfer across the metal oxide interface, enabling surface modulation of supported metals, and, hence, their improved activities [9, 10]. This interaction is commonly thought to be localized within 1 nm around the interface region, owing to the intrinsic limit of charge transfer set by the support [5, 7]. Yet this charge transfer could be in principle regulated through tuning the structure and chemical properties of the support, as detailed in previous reports [6, 8]. An earlier research described that CO oxidation on CeO_2-supported group VIII metals is localized, where the nanoscale perimeter atoms are active sites [8]. Intriguingly, Suchorski et al. have recently showed that ZrO_2 (also Al_2O_3 and other oxides) supported Pd aggregates (50-200 μm) enable high CO tolerance throughout the entire Pd particles owing to the metal oxide interaction effect, leading to remote activation of Pd up to thousands of nanometers [5]. Although current PdS_x-Ni_3S_4'dot-on-rod' structure somewhat differs from the conventional metal oxide heterogeneous catalysts, the substantially enhanced HER performances seen here are also likely the result of long-range activation caused by the PdS_x-Ni_3S_4 interface based on the large electronic property changes of Ni_3S_4 nanorods that uncovered by multiple characterizations. Detailed explanations for this remote activation are still lacking and require further investigations.

In summary, we here demonstrate an unprecedented long-range activation of polydymite Ni_3S_4 nanorods due to the interfacial interaction created by nanoparticulate PdS_x terminations, which results in substantial HER efficiency

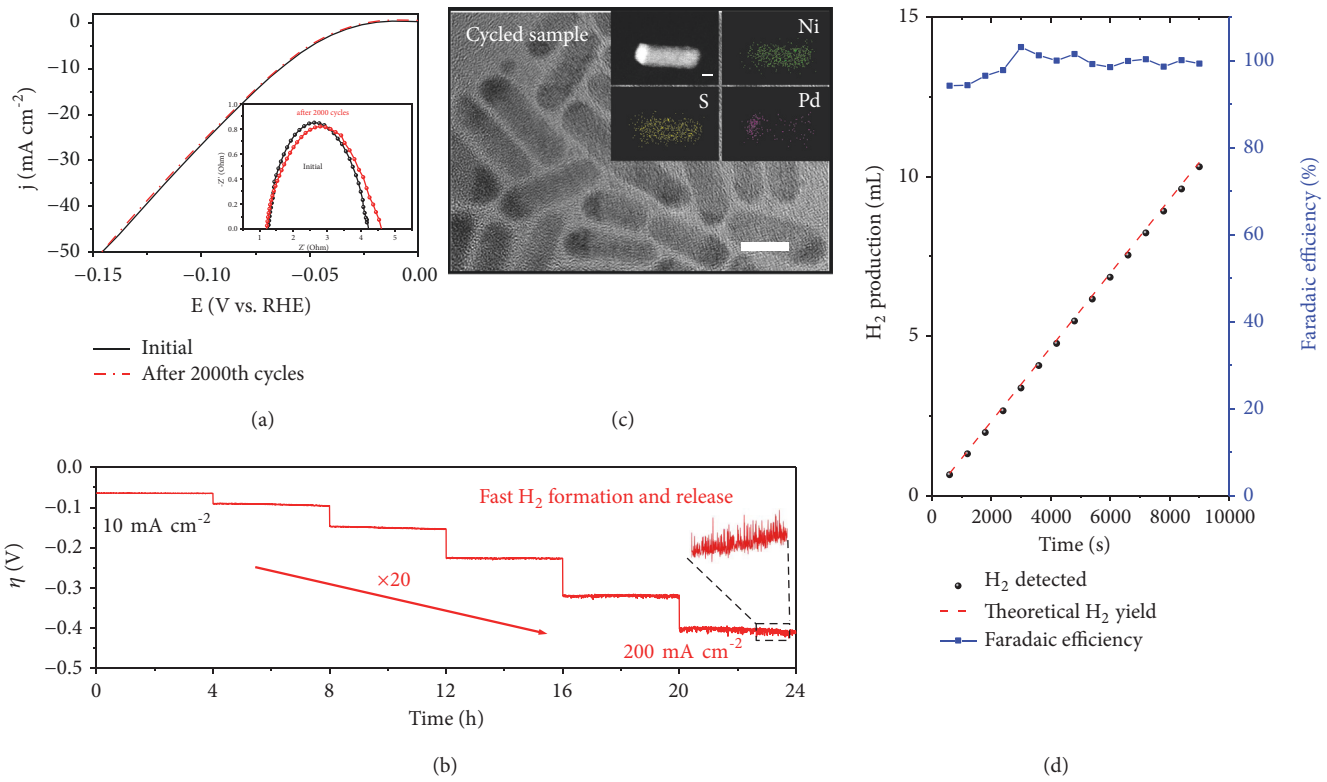


FIGURE 5: *Catalytic stability of PdS_x-Ni_3S_4 heterocatalyst.* (a) HER polarization curves of PdS_x-Ni_3S_4 catalyst before and after 2,000 potential cycles between -200 and 200 mV versus RHE. Inset shows the Nyquist plots before and after stability tests. *The potential for the Nyquist plot measurement was -0.204 V* versus *RHE.* (b) Multistep chronopotentiometric curve for the PdS_x-Ni_3S_4 catalyst, showing that this new heterocatalyst runs robustly even at a high current density of 200 mA cm^{-2}. (c) TEM image (scale bar: 10 nm) and STEM-EDX mapping (inset; scale bar: 5 nm) of PdS_x-Ni_3S_4 heterocatalyst after 2,000 cycles of accelerated stability test, respectively. (d) Current efficiency for H_2 evolution catalyzed by the PdS_x-Ni_3S_4 catalyst, showing a Faradic efficiency close to 100%.

gains. This strong impact on Ni_3S_4 rods with length up to 25 nm arises from the modified surface electronic structure based on various experimental investigations, somewhat analogous to a remote activation observed recently on Pd-oxides catalysts for CO oxidation [5]. We expect that such long-range effect from nanoscopic interfaces is not unique to Ni_3S_4, but bears general implications for other catalyst systems beyond metal chalcogenides. This work provides an unconventional pathway towards a wide range of materials whose performances are highly attractive for electrocatalysis.

4. Materials and Methods

4.1. Synthesis of PdS_X-Ni_3S_4 Heteronanorods. In a typical procedure, 0.05 mmol of $PdCl_2$, 0.2 mmol nickel (II) 2,4-pentanedionate ($Ni(acac)_2$, Alfa Aesar, 99%), and 5 mL oleylamine (OAm) were loaded into a 25 mL three-necked flask under stirring. The mixture was heated under N_2 atmosphere to 100°C and kept at this temperature for 30 mins. And then 0.5 mL 1-dodecanethiol was injected into the solution in sequence. After that the mixture solution was heated to 250°C at a heating rate of 10°C/min and incubated at this temperature for 30 min, generating a black solution. After cooling to room temperature, black precipitate was obtained by adding a large amount of ethanol into the colloidal solution and centrifugated at 10000 rpm for 5 mins. The precipitate was washed three times with excessive ethanol and redispersed in hexane.

4.2. Synthesis of Pure Ni_3S_4 Nanorods. Pure Ni_3S_4 nanorods were synthesized by similar procedures to that described for the synthesis of PdS_x-Ni_3S_4 hybrid nanorods in the absence of 0.05 mmol of $PdCl_2$.

4.3. Characterization. The samples were characterized by different analytic techniques. XRD was performed on a Philips X'Pert Pro Super X-ray diffractometer equipped with graphite-monochromatized Cu Ka radiation (λ = 1.54178 Å). Scanning electron microscope (SEM, Zeiss Supra 40) and JEOL 2010F(s) TEM were applied to investigate the size and morphology. The HRTEM images, EELS, SAED, and EDX elemental mappings were taken on JEMARM 200F Atomic Resolution Analytical Microscope with an acceleration voltage of 200 kV. XPS was performed by an X-ray photoelectron spectrometer (ESCALab MKII) with an excitation source of mg Kα radiation (1253.6 eV). ICP data were obtained by an Optima 7300 DV instrument. Ultraviolet photoelectron spectroscopy was carried out at the BL11U beamline of National Synchrotron Radiation Laboratory in Hefei, China. The X-ray absorption spectra of Ni and S K-edges were

obtained at the beamline 4B7A station of Beijing Synchrotron Radiation Facility (China).

4.4. Electrochemical Measurements. Electrochemical measurements were performed using a Multipotentiostat (IM6ex, ZAHNER elektrik, Germany). All measurements in 0.5 M H_2SO_4 were performed using a three-electrode cell. A graphite rod and Ag/AgCl (PINE, 3.5 M KCl) were used as counter and reference electrodes, respectively. 5 mg of catalyst powder was dispersed in 1 ml isopropanol with 20 μl of Nafion solution (5 wt%, Sigma-Aldrich); then the mixture was ultrasonicated for at least 30 min to generate a homogeneous ink. Next, 200 μl of the dispersion was transferred onto the 1 cm^2 carbon fiber paper, leading to the catalyst loading ~1 mg cm^{-2}. All the potentials in this study were referenced to Ag/AgCl (measured) or the reversible hydrogen electrode (RHE). Before the electrochemical measurement, the electrolyte (0.5 M H_2SO_4) was degassed by bubbling N_2 for 30 min. The polarization curves were obtained by sweeping the potential from -0.7 to 0.2 V versus Ag/AgCl at room temperature with a sweep rate of 5 mV s^{-1}. The accelerated stability tests were performed in N_2-saturated 0.5 M H_2SO_4 at room temperature by potential cycling between -0.2 and 0.2 V versus RHE at a sweep rate of 100 mV s^{-1} for given number of cycles. At the end of each cycling, the resulting electrode was used for polarization curves. Chronoamperometric measurements of the catalysts on carbon fiber paper electrodes kept at a constant current density of 10 mA cm^{-2} in N_2-saturated 0.5 M H_2SO_4. Multistep chronopotentiometric curve for the PdS_x-Ni_3S_4 hybrid nanorods was tested with current density increasing from 10 to 200 mA cm^{-2}. CV measurements taken with various scan rates (20, 40, 60 mV s^{-1}, etc.) were conducted in static solution to estimate the double-layer capacitance by sweeping the potential across the nonfaradaic region 0.1-0.2 V versus RHE Electrochemical impedance spectroscopy measurement was performed when the working electrode was biased at a constant -0.40 V versus Ag/AgCl while sweeping the frequency from 100 kHz to 100 mHz with a 5 mV AC dither.

The values of TOF were calculated by assuming that every metal atom is involved in the catalysis (lower TOF limits were calculated):

$$TOF = \frac{j \times S}{2 \times F \times n} \quad (1)$$

Here, j (mA cm^{-2}) is the measured current density, S is the geometric area of carbon paper, the number 2 means 2 electrons/mol of H_2, F is Faraday constant (96485.3 C mol^{-1}), and n is the moles of coated metal atom on the electrode calculated from the deposited catalysts.

Data Availability

All data needed to evaluate the conclusions in the paper are present in the paper and the Supplementary Materials. Additional data related to this paper may be requested from the authors.

Conflicts of Interest

The authors declare no competing financial interest.

Authors' Contributions

Shu-Hong Yu and Min-Rui Gao supervised the project, conceived the ideas and experiments, analyzed the results, and wrote the paper. Qiang Gao planned and performed the experiments, collected and analyzed the data, and wrote the paper. Rui Wu, Yang Liu, Li-Mei Shang, and Yi-Ming Ju helped with synthesis of the materials and collected the data. Ya-Rong Zheng, Yi Li, Chao Gu, and Jian-Wei Liu assisted with the experiments and characterizations. Xu-Sheng Zheng and Jun-Fa Zhu performed the UPS measurements. All authors discussed the results and commented on the manuscript. Qiang Gao and Rui Wu contributed equally to this work.

Acknowledgments

We acknowledge the funding support from the National Natural Science Foundation of China (Grants 21521001, 21431006, 21225315, 21321002, 91645202, 51702312, and 51802301), the Users with Excellence and Scientific Research Grant of Hefei Science Center of CAS (2015HSCUE007), the Key Research Program of Frontier Sciences, CAS (Grant QYZDJ-SSWSLH036), the Chinese Academy of Sciences (Grants KGZDEW-T05, XDA090301001), the Fundamental Research Funds for the Central Universities (WK2060190045, WK2340000076), and the Recruitment Program of Global Youth Experts. We would like to thank the beamline 1W1B station in the Beijing Synchrotron Radiation Facility and BL14W1 at the Shanghai Synchrotron Radiation Facility for help with the characterizations. This work was partially carried out at the USTC Center for Micro and Nanoscale Research and Fabrication.

Supplementary Materials

Figure S1: HRTEM characterization. Figure S2: HRTEM and FFT characterizations. Figure S3: EDS spectrum of the PdS_x-Ni_3S_4 heteronanorods. Figure S4: STEM-EDX elemental mapping of a single PdS_x-Ni_3S_4 heteronanorod. Figure S5: EDS line analysis of a typical PdS_x-Ni_3S_4 heteronanorod. Figure S6: size characterizations. Figure S7: TEM images of the products synthesized by using different amount of 1-dodecanethiol. Figure S8: TEM images of products obtained at different temperature. Figure S9: TEM images of the products synthesized with different Pd:Ni radio. Figure S10: TEM images of the products synthesized at 250°C for different reaction time. Figure S11: TEM images of pure Ni_3S_4 nanorods. Figure S12: The SAED patterns of PdS_x-Ni_3S_4 and pure Ni_3S_4 nanorods. Figure S13: Characterization of Pd precursor and pure PdS_x nanoparticles. Figure S14: XPS spectra analysis. Figure S15: FT-IR spectra of PdS_x-Ni_3S_4 heteronanorods before and after acetic acid treatment. Figure S16: HER performance for the products obtained at different reaction time and the products obtained with

different ratio of Pd:Ni. Figure S17: HER performance for the products obtained with different amount of $C_{12}SH$ and the products obtained at different temperatures. Figure S18: comparison of the onset potential required to start the HER on various Ni-based electrocatalysts. Figure S19: Tafel plot for the Pt/C (20 wt%) benchmark. Figure S20: exchange current density for different studied catalysts. Figure S21: capacitance measurement. Figure S22: Capacitance measurement. Figure S23: EDS spectrum of the PdS_x-Ni_3S_4 heteronanorods after 2000 cyclic voltammetry cycles. Figure S24: XPS spectra for the PdS_x-Ni_3S_4 heterocatalysts before and after 2000 potential cycles. Table S1: comparison of catalytic parameter of different Pt-free HER catalysts. *(Supplementary Materials)*

References

[1] L. Schlapbach, "Technology: Hydrogen-fuelled vehicles," *Nature*, vol. 460, no. 7257, pp. 809–811, 2009.

[2] M. Cabán-Acevedo, M. L. Stone, J. R. Schmidt et al., "Efficient hydrogen evolution catalysis using ternary pyrite-type cobalt phosphosulphide," *Nature Materials*, vol. 14, no. 12, pp. 1245–1251, 2015.

[3] M. S. Faber and S. Jin, "Earth-abundant inorganic electrocatalysts and their nanostructures for energy conversion applications," *Energy & Environmental Science*, vol. 7, no. 11, pp. 3519–3542, 2014.

[4] M.-R. Gao, Y.-F. Xu, J. Jiang, and S.-H. Yu, "Nanostructured metal chalcogenides: Synthesis, modification, and applications in energy conversion and storage devices," *Chemical Society Reviews*, vol. 42, no. 7, pp. 2986–3017, 2013.

[5] Y. Suchorski, S. M. Kozlov, I. Bespalov et al., "The role of metal/oxide interfaces for long-range metal particle activation during CO oxidation," *Nature Materials*, vol. 17, no. 6, pp. 519–522, 2018.

[6] S. Kattel, P. Liu, and J. G. Chen, "Tuning selectivity of CO_2 hydrogenation reactions at the metal/oxide interface," *Journal of the American Chemical Society*, vol. 139, no. 29, pp. 9739–9754, 2017.

[7] Y. Lykhach, S. M. Kozlov, T. Skála et al., "Counting electrons on supported nanoparticles," *Nature Materials*, vol. 15, no. 3, pp. 284–288, 2016.

[8] M. Cargnello, V. V. T. Doan-Nguyen, T. R. Gordon et al., "Control of metal nanocrystal size reveals metal-support interface role for ceria catalysts," *Science*, vol. 341, no. 6147, pp. 771–773, 2013.

[9] C. T. Campbell, "Electronic perturbations," *Nature Chemistry*, vol. 4, no. 8, pp. 597-598, 2012.

[10] A. Bruix, J. A. Rodriguez, P. J. Ramírez et al., "A new type of strong metal-support interaction and the production of H_2 through the transformation of water on $Pt/CeO_2(111)$ and $Pt/CeOx/TiO_2(110)$ catalysts," *Journal of the American Chemical Society*, vol. 134, no. 21, pp. 8968–8974, 2012.

[11] A. T. Bell, "The impact of nanoscience on heterogeneous catalysis," *Science*, vol. 299, no. 5613, pp. 1688–1691, 2003.

[12] S. J. Tauster, "Strong metal-support interactions," *Accounts of Chemical Research*, vol. 20, no. 11, pp. 389–394, 1987.

[13] S. J. Tauster, S. C. Fung, R. T. K. Baker, and J. A. Horsley, "Strong interactions in supported-metal catalysts," *Science*, vol. 211, no. 4487, pp. 1121–1125, 1981.

[14] S. J. Tauster, S. C. Fung, and R. L. Garten, "Strong metal-support interactions. Group 8 noble metals supported on titanium dioxide," *Journal of the American Chemical Society*, vol. 100, no. 1, pp. 170–175, 1978.

[15] G. N. Vayssilov, Y. Lykhach, A. Migani et al., "Support nanostructure boosts oxygen transfer to catalytically active platinum nanoparticles," *Nature Materials*, vol. 10, no. 4, pp. 310–315, 2011.

[16] Y. Liang, Y. Li, H. Wang, and H. Dai, "Strongly coupled inorganic/nanocarbon hybrid materials for advanced electrocatalysis," *Journal of the American Chemical Society*, vol. 135, no. 6, pp. 2013–2036, 2013.

[17] M.-R. Gao, Y.-F. Xu, J. Jiang, Y.-R. Zheng, and S.-H. Yu, "Water oxidation electrocatalyzed by an efficient $Mn_3O_4/CoSe_2$ nanocomposite," *Journal of the American Chemical Society*, vol. 134, no. 6, pp. 2930–2933, 2012.

[18] R. Subbaraman, D. Tripkovic, D. Strmcnik et al., "Enhancing hydrogen evolution activity in water splitting by tailoring Li^+-$Ni(OH)_2$-Pt interfaces," *Science*, vol. 334, no. 6060, pp. 1256–1260, 2011.

[19] W. Lubitz, H. Ogata, O. Rüdiger, and E. Reijerse, "Hydrogenases," *Chemical Reviews*, vol. 114, no. 8, pp. 4081–4148, 2014.

[20] M. Gao, M. K. Chan, and Y. Sun, "Edge-terminated molybdenum disulfide with a 9.4-Å interlayer spacing for electrochemical hydrogen production," *Nature Communications*, vol. 6, no. 1, 2015.

[21] T. F. Jaramillo, K. P. Jørgensen, J. Bonde, J. H. Nielsen, S. Horch, and I. Chorkendorff, "Identification of active edge sites for electrochemical H_2 evolution from MoS_2 nanocatalysts," *Science*, vol. 317, no. 5834, pp. 100–102, 2007.

[22] B. Hinnemann, P. G. Moses, J. Bonde et al., "Biomimetic hydrogen evolution: MoS_2 nanoparticles as catalyst for hydrogen evolution," *Journal of the American Chemical Society*, vol. 127, no. 15, pp. 5308-5309, 2005.

[23] X. Long, G. Li, Z. Wang et al., "Metallic iron-nickel sulfide ultrathin nanosheets as a highly active electrocatalyst for hydrogen evolution reaction in acidic media," *Journal of the American Chemical Society*, vol. 137, no. 37, pp. 11900–11903, 2015.

[24] M. S. Faber, M. A. Lukowski, Q. Ding, N. S. Kaiser, and S. Jin, "Earth-abundant metal pyrites (FeS_2, CoS_2, NiS_2, and their alloys) for highly efficient hydrogen evolution and polysulfide reduction electrocatalysis," *The Journal of Physical Chemistry C*, vol. 118, no. 37, pp. 21347–21356, 2014.

[25] Y.-R. Zheng, M.-R. Gao, Z.-Y. Yu, Q. Gao, H.-L. Gao, and S.-H. Yu, "Cobalt diselenide nanobelts grafted on carbon fiber felt: an efficient and robust 3D cathode for hydrogen production," *Chemical Science*, vol. 6, no. 8, pp. 4594–4598, 2015.

[26] M.-R. Gao, J.-X. Liang, Y.-R. Zheng et al., "An efficient molybdenum disulfide/cobalt diselenide hybrid catalyst for electrochemical hydrogen generation," *Nature Communications*, vol. 6, 2015.

[27] D. Kong, H. Wang, Z. Lu, and Y. Cui, "CoSe2 nanoparticles grown on carbon fiber paper: An efficient and stable electrocatalyst for hydrogen evolution reaction," *Journal of the American Chemical Society*, vol. 136, no. 13, pp. 4897–4900, 2014.

[28] M. S. Faber, R. Dziedzic, M. A. Lukowski, N. S. Kaiser, Q. Ding, and S. Jin, "High-performance electrocatalysis using metallic cobalt pyrite (CoS_2) micro- and nanostructures," *Journal of the American Chemical Society*, vol. 136, no. 28, pp. 10053–10061, 2014.

[29] L.-L. Feng, G. Yu, Y. Wu et al., "High-index faceted Ni_3S_2 nanosheet arrays as highly active and ultrastable electrocatalysts for water splitting," *Journal of the American Chemical Society*, vol. 137, no. 44, pp. 14023–14026, 2015.

[30] R. Karthikeyan, M. Navaneethan, J. Archana, D. Thangaraju, M. Arivanandhan, and Y. Hayakawa, "Shape controlled synthesis of hierarchical nickel sulfide by the hydrothermal method," *Dalton Transactions*, vol. 43, no. 46, pp. 17445–17452, 2014.

[31] Y. Tan, M. Liang, P. Lou et al., "In situ fabrication of CoS and NiS nanomaterials anchored on reduced graphene oxide for reversible lithium storage," *ACS Applied Materials & Interfaces*, vol. 8, no. 23, pp. 14488–14493, 2016.

[32] H. Fan, H. Yu, X.-L. Wu et al., "Controllable preparation of square nickel chalcogenide (NiS and $NiSe_2$) nanoplates for superior li/na ion storage properties," *ACS Applied Materials & Interfaces*, 2016.

[33] S. Ni, X. Yang, and T. Li, "Fabrication of a porous NiS/Ni nanostructured electrode via a dry thermal sulfuration method and its application in a lithium ion battery," *Journal of Materials Chemistry*, vol. 22, no. 6, pp. 2395–2397, 2012.

[34] Z. Zhang, Q. Wang, C. Zhao, S. Min, and X. Qian, "One-step hydrothermal synthesis of 3D petal-like Co_9S_8/RGO/Ni_3S_2 composite on nickel foam for high-performance supercapacitors," *ACS Applied Materials & Interfaces*, vol. 7, no. 8, pp. 4861–4868, 2015.

[35] J. Yang, X. Duan, Q. Qin, and W. Zheng, "Solvothermal synthesis of hierarchical flower-like β-NiS with excellent electrochemical performance for supercapacitors," *Journal of Materials Chemistry A*, vol. 1, no. 27, pp. 7880–7884, 2013.

[36] C.-S. Dai, P.-Y. Chien, J.-Y. Lin et al., "Hierarchically structured Ni_3S_2/carbon nanotube composites as high performance cathode materials for asymmetric supercapacitors," *ACS Applied Materials & Interfaces*, vol. 5, no. 22, pp. 12168–12174, 2013.

[37] R. Cid, J. Neira, J. Godoy, J. M. Palacios, and A. López Agudo, "Thiophene hydrodesulfurization on sulfided nickel-exchanged USY zeolites. Effect of the pH of the catalyst preparation," *Applied Catalysis A: General*, vol. 125, no. 1, pp. 169–183, 1995.

[38] Y. Wu, G.-D. Li, Y. Liu et al., "Overall water splitting catalyzed efficiently by an ultrathin nanosheet-built, hollow Ni_3S_2-based electrocatalyst," *Advanced Functional Materials*, vol. 26, no. 27, pp. 4839–4847, 2016.

[39] J. M. Falkowski, N. M. Concannon, B. Yan, and Y. Surendranath, "Heazlewoodite, Ni_3S_2: a potent catalyst for oxygen reduction to water under benign conditions," *Journal of the American Chemical Society*, vol. 137, no. 25, pp. 7978–7981, 2015.

[40] C. An, Z. Zhang, X. Chen, and Y. Liu, "Selective synthesis of Ni_3S_4 nanocrystallites with hollow structures through a solution-phase approach," *Materials Letters*, vol. 60, no. 29-30, pp. 3631–3634, 2006.

[41] A. Manthiram and Y. U. Jeong, "Ambient temperature synthesis of spinel Ni_3S_4: an itinerant electron ferrimagnet," *Journal of Solid State Chemistry*, vol. 147, no. 2, pp. 679–681, 1999.

[42] Y. U. Jeong and A. Manthiram, "Synthesis of nickel sulfides in aqueous solutions using sodium dithionite," *Inorganic Chemistry*, vol. 40, no. 1, pp. 73–77, 2001.

[43] Y. Shemesh, J. E. MacDonald, G. Menagen, and U. Banin, "Synthesis and photocatalytic properties of a family of CdS-PdX hybrid nanoparticles," *Angewandte Chemie International Edition*, vol. 50, no. 5, pp. 1185–1189, 2011.

[44] T. Teranishi, M. Saruyama, M. Nakaya, and M. Kanehara, "Anisotropically phase-segregated Pd-Co-Pd sulfide nanoparticles formed by fusing two Co-Pd sulfide nanoparticles," *Angewandte Chemie International Edition*, vol. 46, no. 10, pp. 1713–1715, 2007.

[45] T. Teranishi, Y. Inoue, M. Nakaya, Y. Oumi, and T. Sano, "Nanoacorns: Anisotropically phase-segregated CoPd sulfide nanoparticles," *Journal of the American Chemical Society*, vol. 126, no. 32, pp. 9914-9915, 2004.

[46] J. Wang, L. Gan, W. Zhang et al., "In situ formation of molecular Ni-Fe active sites on heteroatom-doped graphene as a heterogeneous electrocatalyst toward oxygen evolution," *Science Advances*, vol. 4, no. 3, Article ID eaap7970, 2018.

[47] X. Zhang, Z. Luo, P. Yu et al., "Lithiation-induced amorphization of Pd3P2S8 for highly efficient hydrogen evolution," *Nature Catalysis*, vol. 1, no. 6, pp. 460–468, 2018.

[48] B. Lassalle-Kaiser, D. Merki, H. Vrubel et al., "Evidence from in situ X-ray absorption spectroscopy for the involvement of terminal disulfide in the reduction of protons by an amorphous molybdenum sulfide electrocatalyst," *Journal of the American Chemical Society*, vol. 137, no. 1, pp. 314–321, 2015.

[49] N. Kornienko, J. Resasco, N. Becknell et al., "Operando spectroscopic analysis of an amorphous cobalt sulfide hydrogen evolution electrocatalyst," *Journal of the American Chemical Society*, vol. 137, no. 23, pp. 7448–7455, 2015.

[50] M. A. Lukowski, A. S. Daniel, F. Meng, A. Forticaux, L. Li, and S. Jin, "Enhanced hydrogen evolution catalysis from chemically exfoliated metallic MoS_2 nanosheets," *Journal of the American Chemical Society*, vol. 135, no. 28, pp. 10274–10277, 2013.